Acta Pharmaceutica Sinica B 2025;15(10):5312−5326

Chinese Pharmaceutical Association
Institute of Materia Medica, Chinese Academy of Medical Sciences

Acta Pharmaceutica Sinica B

www.elsevier.com/locate/apsb
www.sciencedirect.com

ORIGINAL ARTICLE

Discovery of orally active and serine-targeting covalent inhibitors against hCES2A for ameliorating irinotecan-triggered gut toxicity

Ya Zhang[a,b,†], Yufan Fan[a,†], Yunqing Song[a,†], Guanghao Zhu[a,†], Xinjuan Li[c,†], Jian Huang[a], Xinrui Guo[d], Changhai Luan[a], Dongning Kang[d], Lu Chen[a,d], Zhangping Xiao[e], Zhaobin Guo[a], Hairong Zeng[a,*], Dapeng Chen[a,d,*], Zhipei Sang[a,c,*], Guangbo Ge[a,*]

[a]*State Key Laboratory of Discovery and Utilization of Functional Components in Traditional Chinese Medicine; Shanghai Frontiers Science Center of TCM Chemical Biology; Institute of Interdisciplinary Integrative Medicine Research, Shanghai University of Traditional Chinese Medicine, Shanghai 201203, China*
[b]*Department of Pharmacy, Jingan District Zhabei Central Hospital, Shanghai 200070, China*
[c]*Key Laboratory of Tropical Biological Resources of Ministry of Education and One Health Institute, Hainan One Health Key Laboratory, School of Pharmaceutical Sciences, Hainan University, Haikou 570228, China*
[d]*Dalian Medical University, Dalian 116044, China*
[e]*Department of Chemistry, Imperial College London W12 0BZ, UK*

Received 6 May 2025; received in revised form 9 June 2025; accepted 9 July 2025

KEY WORDS

Human carboxylesterase 2 (hCES2A);
Structure-based drug design (SBDD);
Donepezil derivatives;
Structure−activity relationship (SAR);
Covalent inhibitors;
Drug repurposing;

Abstract Human carboxylesterase 2A (hCES2A) plays pivotal roles in prodrug activation and hydrolytic metabolism of ester-bearing chemicals. Targeted inhibition of intestinal hCES2A represents a feasible strategy to mitigate irinotecan-triggered gut toxicity (ITGT), but the orally active, selective, and efficacious hCES2A inhibitors are rarely reported. Here, a novel drug-like hCES2A inhibitor was developed *via* three rounds of structure-based drug design (SBDD) and structural optimization. Initially, donepezil was identified as a moderate hCES2A inhibitor from 2000 US Food and Drug Administration (FDA)-approved drugs. Following two rounds of SBDD and structural optimization, a donepezil derivative (**B7**) was identified as a strong reversible hCES2A inhibitor. Subsequently, nine **B7** carbamates were rationally designed, synthesized and biologically assayed. Among all synthesized carbamates, **C3** showed the most potent time-dependent inhibition on hCES2A (IC_{50} = 0.56 nmol/L), excellent specificity and

*Corresponding authors.
E-mail addresses: zenghairong@shutcm.edu.cn (Hairong Zeng), friendchen@dmu.edu.cn (Dapeng Chen), sangzhipei@hainanu.edu.cn (Zhipei Sang), geguangbo@shutcm.edu.cn (Guangbo Ge).
[†]These authors made equal contributions to this work.
Peer review under the responsibility of Chinese Pharmaceutical Association and Institute of Materia Medica, Chinese Academy of Medical Sciences.

https://doi.org/10.1016/j.apsb.2025.08.007

Carbamates;
Irinotecan-triggered gut toxicity (ITGT)

favorable drug-like properties. **C3** could covalently modify the catalytic serine of hCES2A with high selectivity, while this agent also showed favorable safety profiles, high intestinal exposure, and impressive effects for ameliorating ITGT in both human intestinal organoids and tumor-bearing mice. Collectively, this study showcases a rational strategy for developing drug-like and serine-targeting covalent inhibitors against target serine hydrolase(s), while **C3** emerges as a promising orally active drug candidate for ameliorating ITGT.

1. Introduction

Mammalian carboxylesterases (CES), the key members of the serine hydrolase superfamily, catalyse the hydrolysis of various xenobiotics and endogenous substances bearing ester- or amide-bond(s), including therapeutic agents (*e.g.*, irinotecan and prasugrel) and environmental toxicants (*e.g.*, pyrethroids and carbamates)[1-3]. Human carboxylesterases 1A (hCES1A) and human carboxylesterases 2 (hCES2A) are two abundant and important CES isoenzymes in humans. Generally, hCES1A is primarily found in hepatocytes and adipocytes, while hCES2A is mainly distributed in epithelial cells of the small intestine and colon[4,5]. As a predominant CES enzyme in the intestinal tract, hCES2A plays crucial roles in the first-pass metabolism and hydrolytic activation of some important ester-bearing agents[6,7]. Accumulating evidence has suggested that hCES2A inhibitors can strongly modulate the oral bioavailability and the *in vivo* effects of hCES2A-substrate drugs[8-10]. Notably, the anticancer agent irinotecan could be readily hydrolyzed by intestinal hCES2A to release the highly toxic metabolite (SN-38), while over-accumulation of SN-38 in the gut may trigger severe delayed diarrhea[11-13]. Currently, loperamide (LPA, a selective μ opioid receptor agonist with moderate hCES2A inhibition) remains the only clinically available agent for mitigating irinotecan-triggered gut toxicity (ITGT). However, its clinical utility is significantly limited by suboptimal anti-hCES2A potency and concerning adverse effects, including cardiac arrhythmias, physical dependence, and central opioid effects[14,15]. These limitations underscore the urgent need to develop more potent hCES2A inhibitors with improved safety profiles and optimal drug-like properties.

Over the past few decades, numerous natural and synthetic compounds with anti-hCES2A activity have been identified[16-22], but orally active, potent, and selective hCES2A inhibitors with favourable safety profiles and optimal drug-likeness properties remain rarely reported. Most previously reported reversible inhibitors of hCES2A exhibit relatively weak anti-hCES2A effects (IC_{50} values in the micromolar range), poor metabolic stability, and unsatisfying cell-membrane permeability[23-26]. Remarkably, most reported reversible hCES2A inhibitors exhibit weak efficacy in rodent models, due to significant species differences in amino acid sequence identity and inhibitor susceptibility among mammalian CES2A enzymes. By contrast, covalent drugs incorporate a mildly reactive group that exploits the conserved catalytic serine residue of serine hydrolases to form irreversible or slowly reversible bonds[27,28]. This mechanism allows medicinal chemists to design the covalent inhibitors of serine hydrolase(s) with prolonged target engagement, exceptional potency, and enhanced selectivity. Although several covalent hCES2A inhibitors (such as organophosphates and carbamates) have been reported with potent anti-hCES2A activity and favorable cell membrane permeability, they often lack selectivity and raise significant safety concerns, particularly with organophosphates[17,29]. These limitations underscore the critical need to develop next-generation CES2A covalent inhibitors demonstrating high selectivity, improved safety profiles, and cross-species efficacy. Given that hCES2A is abundantly expressed in the endoplasmic reticulum of intestinal epithelial cells, an ideal orally administered hCES2A inhibitor should meet the following key criteria: 1) ultrahigh anti-hCES2A potency; 2) excellent specificity; 3) efficient cell-membrane permeability; 4) favourable safety profiles; 5) high intestinal exposure[30-32].

This study aimed to develop ideal orally active hCES2A-targeted covalent inhibitors demonstrating high potency, excellent selectivity, and favourable drug-like properties (Scheme 1A). First, structure-based virtual screening (SBVS) of 2000 US Food and Drug Administration (FDA)-approved drugs was performed to identify potential hCES2A inhibitors. Anti-hCES2A activity assays revealed that donepezil (a marketed acetylcholinesterase inhibitor) exhibited moderate inhibitory activity against hCES2A. Subsequently, three rounds of structure-based drug design (SBDD) and structure−activity relationship (SAR) studies were conducted to optimize the anti-hCES2A potency and drug-like properties. In the 1st round structural optimization (Scheme 1B), scaffold hopping of donepezil yielded **A3** as a more potent hCES2A inhibitor (IC_{50} = 0.92 μmol/L). The 2nd of SBDD and SAR analysis identified **B7** as a potent reversible hCES2A inhibitor (IC_{50} = 0.11 μmol/L), with the C-2 phenolic group positioned within 5 Å of the catalytic Ser-228 residue (Scheme 1C). This spatial proximity inspired us to design a suite of carbamate derivatives as serine-targeting covalent inhibitors of hCES2A. The 3rd round (Scheme 1D) revealed **C3** and its analogues as highly potent and irreversible covalent inhibitors of hCES2A (IC_{50} = 0.56 nmol/L for **C3** following 33 min pre-incubation). These findings motivated us to perform comprehensive *in vitro* and *in vivo* assays to uncover the anti-hCES2A mechanisms of **C3**, assess its inhibitory effects in living cells, and examine its safety profiles and treatment outcomes for ameliorating ITGT in tumor-bearing mice.

2. Results and discussion

2.1. Discovery of donepezil derivatives as hCES2A inhibitors

Increasing evidence has showed that drug repurposing is an efficient way to rapidly identify drug-like hit compounds with specific biological activities and enhanced therapeutic potentials[33-36]. In this work, SBVS was firstly used for identifying drug-like compounds from 2000 FDA-approved drugs as potential

hCES2A inhibitors[37]. As shown in Fig. 1A and Supporting Information Table S1, after SBVS-assisted navigation, a total of 36 FDA-approved drugs were found with high binding affinities (<−8.0 kcal/mol) towards hCES2A, which were identified as potential hCES2A binders[38]. Anti-hCES2A assays showed that 11 entities of 36 FDA-approved drugs were hCES2A inhibitors. Donepezil (a selective inhibitor of human acetylcholinesterase) was identified as the most potent hCES2A inhibitor with a IC_{50} value of 3.91 μmol/L (Fig. 1B).

Next, 2D interaction analysis was performed to explore the key fragments of donepezil for hCES2A binding. As shown in Fig. 1C and Supporting Information Fig. S1, the indanone and phenyl groups of donepezil created a hydrogen bond and hydrophobic interactions with hCES2A, respectively, but the piperidine ring did not create any interactions with hCES2A. These observations suggested that the indanone and phenyl moiety were more likely as the key pharmacophores for hCES2A inhibition. To validate this assumption, both **A1** and **A2** were designed and synthesized. As expected, **A1** (the indanone and phenyl moiety coupling with a piperidine ring) could not inhibit hCES2A even at a high dose (>500 μmol/L), while **A2** conserved the anti-hCES2A activity at the same level as donepezil. These findings suggested that the piperidine ring showed unbeneficial effects for hCES2A inhibition. It was also found that introducing a double bond at the α site of the carbonyl group significantly enhanced anti-hCES2A activity, as evidenced by the IC_{50} values of **A3** (0.92 μmol/L) *vs.* **A2** (7.16 μmol/L). By contrast, removing one or two methoxy groups at the C-5 or C-6 site on the indanone ring is unbeneficial for hCES2A inhibition. Meanwhile, a suite of **A3** derivatives (**A6**−**A15**) was designed and synthesized *via* replacing the right phenyl moiety (A ring) of **A3** with saturated ring, heteroaromatic ring, anthracene, naphthalene, or biphenyl moiety (Fig. 1D, Supporting Information Fig. S2 and Supporting Information Table S2). Unfortunately, all these newly designed **A3** derivatives showed lesser anti-hCES2A activity (decreased by 1.38−20.40 folds). Docking simulations showed that **A3** could be well-fitted into the catalytic cavity of hCES2A (Fig. 1E), the 4′-methoxyl of **A3** created carbon-hydrogen bonding with Gly-148, while the B ring of **A3** generated strong interactions with Phe-153 *via* π−π interactions (Fig. 1F and G). It was also found that the right phenyl moiety (A ring) of **A3** could also generate hydrophobic interactions with some key residues (such as Met-354, Ile-350, and Ala-150) in the catalytic cavity of hCES2A. These findings suggest that both the A ring and the methoxy groups on the B ring of donepezil derivatives are beneficial for hCES2A inhibition, suggesting that **A3** acts as a favorable core scaffold for constructing hCES2A inhibitors.

2.2. *SAR study of **A3** derivatives*

To further improve the anti-hCES2A potency of **A3**, a suite of **A3** derivatives (**B1**−**B25**) was designed by incorporating various substitutions on the A ring of **A3**. As illustrated in Fig. 2A, Supporting Information Figs. S3 and S4, and Supporting Information Table S3, introducing a halogen atom at the C-2 or C-4 site significantly weakened the anti-hCES2A activity, as evidenced by **B1** (IC_{50} = 20.91 μmol/L), **B2** (IC_{50} = 12.10 μmol/L), and **B3** (IC_{50} = 2.97 μmol/L). Adding a methoxy group at the C-2, C-3, or C-4 site substantially diminished the anti-hCES2A effects, as demonstrated by the IC_{50} values of **B4** (IC_{50} = 5.50 μmol/L), **B5** (IC_{50} = 64.76 μmol/L), and **B6** (IC_{50} = 17.87 μmol/L). Remarkably, introducing a phenolic group at the C-2 site (**B7**) strongly enhanced the anti-hCES2A effect by 8.36 folds, showing an IC_{50} value of 0.11 μmol/L. By contrast, introducing a phenolic group at the C-3 (**B8**) or C-4 position (**B9**) would slightly reduce the anti-hCES2A activity. Introducing a methyl (**B11**), a nitro group (**B13**), or a nitrogen heterocyclic ring at the C-2 position (**B14** and **B15**) slightly enhanced the anti-hCES2A effects. A suite of disubstituted **A3** derivatives were also synthesized. As shown in Fig. 2A, most disubstituted **A3** derivatives displayed relatively

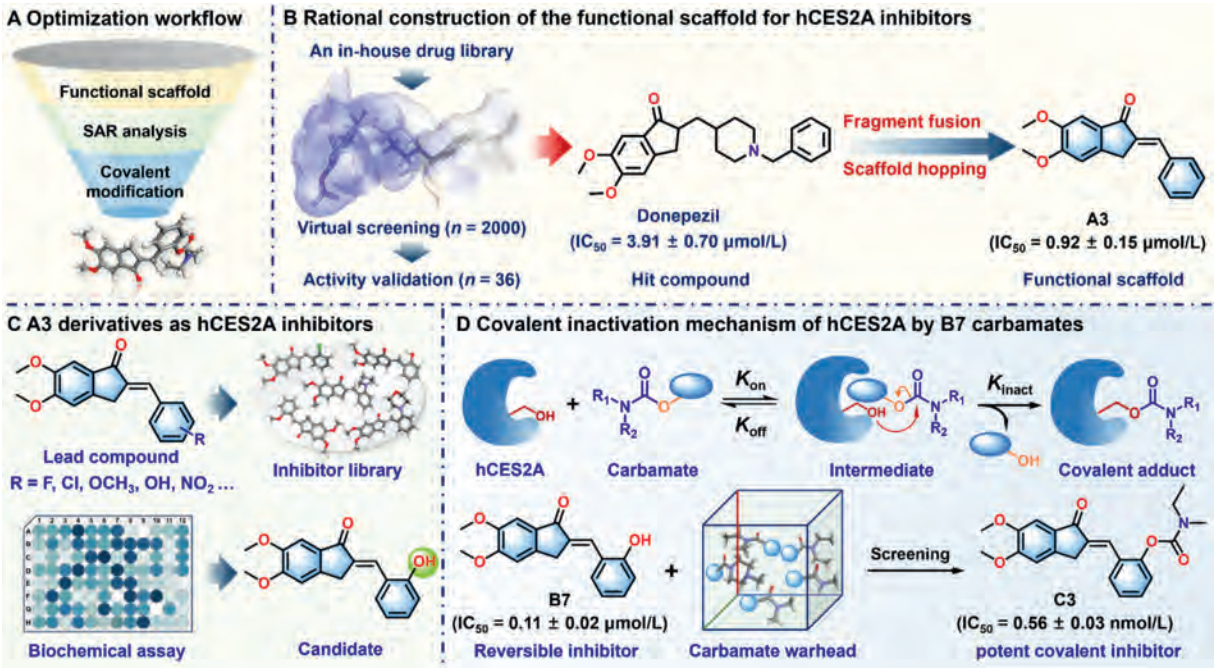

Scheme 1 Discovery of a novel orally active, selective, and potent hCES2A covalent inhibitor for ameliorating ITGT.

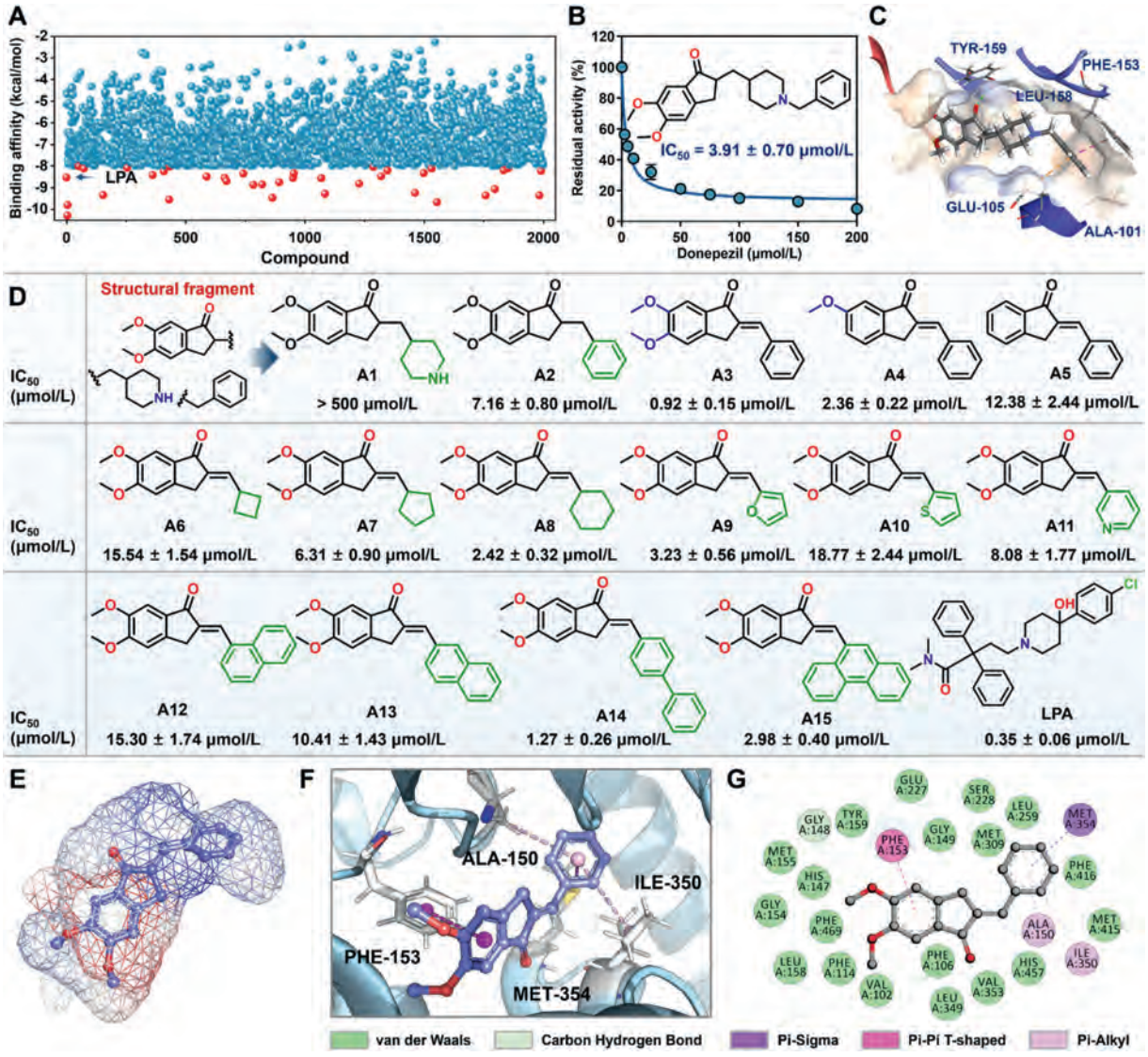

Figure 1 Seeking the core scaffold for developing hCES2A inhibitors *via* integrating structure-based virtual screening (SBVS) and fluorescence-based high-throughput inhibitor screening. (A) The predicted binding-affinity scores of 2000 FDA-approved drugs *via* docking simulations. (B) Dose-dependent inhibition curve of donepezil. (C) Binding modes and 2D interaction analysis of donepezil in hCES2A (AlphaFold ID: O00748). (D) Structures and IC_{50} values of donepezil derivatives against hCES2A. (E) Binding surface of **A3** in the catalytic cavity of hCES2A. (F) Binding pose and detailed view of **A3** and hCES2A. (G) 2D interactions between **A3** and the residues surrounding the catalytic cavity of hCES2A.

weak anti-hCES2A activities, while **B20** (IC_{50} = 0.29 μmol/L) and **B21** (IC_{50} = 0.40 μmol/L) displayed enhanced anti-hCES2A activities compared to **A3** (0.92 μmol/L). These findings clearly demonstrated that introducing a phenolic group at the C-2 site strongly enhanced the anti-hCES2A effects of donepezil derivatives.

Docking simulations showed that **B7** could be well-fitted into the catalytic cavity of hCES2A, while the C-2 phenolic group of **B7** could form a hydrogen bond with the catalytic residue (Ser-228) of hCES2A with a measured distance of 2.4 Å (Fig. 2B and C), which well-explained the improved anti-hCES2A activity of this agent. Since donepezil derivatives may also act as human acetylcholinesterase (hAChE) inhibitors, it is necessary to test the anti-hAChE activities of both **B7** and **A3** (Supporting Information Fig. S5). The results show that **B7** showed very weak anti-hAChE activity, which inspired us to design more potent and selective hCES2A inhibitors by using **B7** as a lead compound.

2.3. *B7 carbamates as novel covalent hCES2A inhibitors*

In view of the suitable positioning and strong interactions between the C-2 phenolic group of **B7** and Ser-228, it is feasible to develop the hCES2A covalent inhibitors by introducing a suitable electrophilic warhead at the C-2 phenolic group[39,40]. It is well-known that carbamates are a class of preferred electrophilic warheads for developing potent covalent inhibitors against mammalian serine hydrolases[41-43], owing to their inherent advantages including desirable water-solubility, improved metabolic stability, and favourable cell-membrane permeability[44]. Theoretically, the highly selective and reactive carbamate electrophile warhead

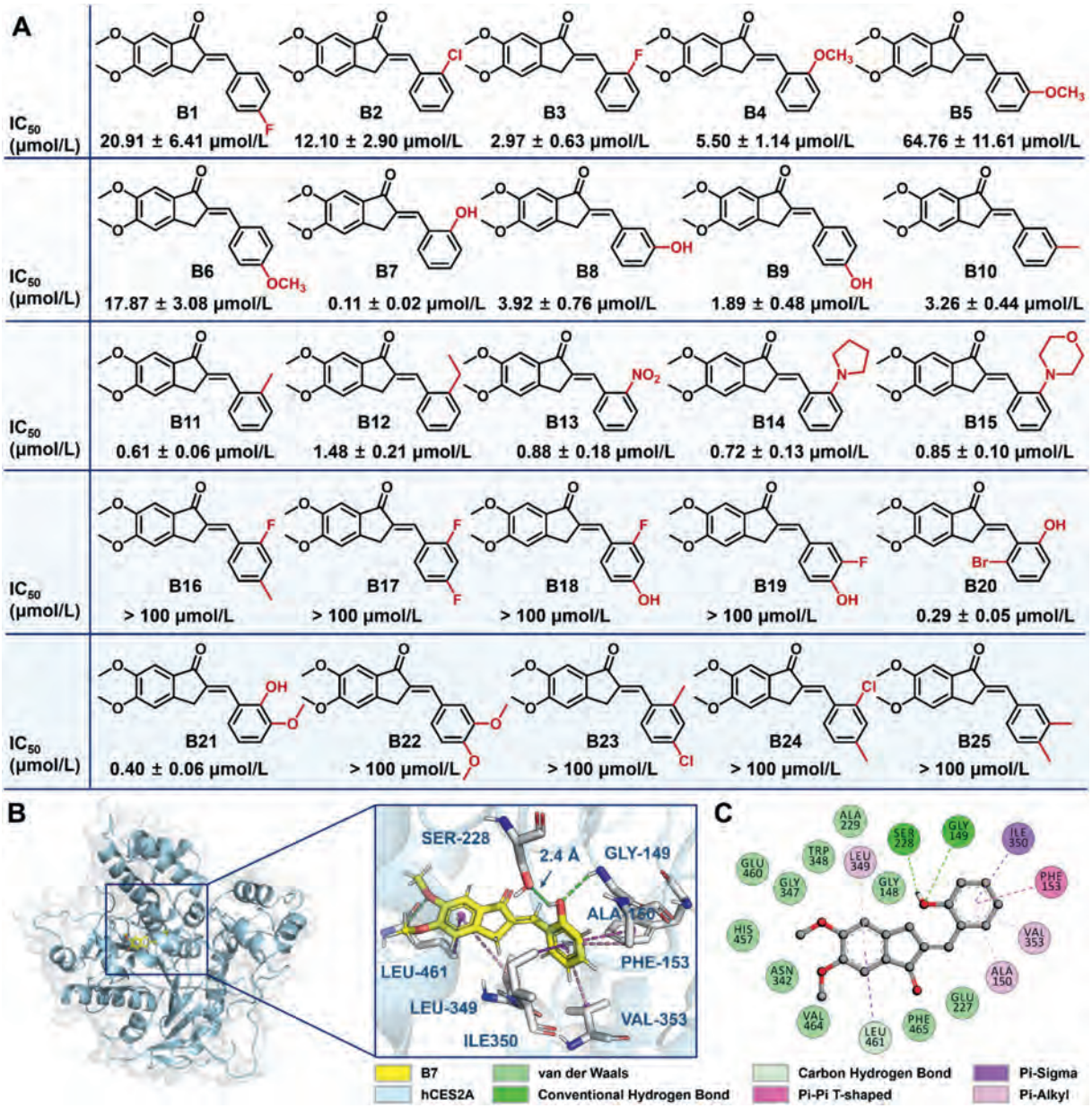

Figure 2 SAR study of **A3** derivatives as hCES2A inhibitors. (A) Chemical structures and the anti-hCES2A activity of donepezil-fused derivatives. (B) The predicted binding mode of **B7** with hCES2A (AlphaFold ID: O00748). (C) 2D interaction analysis of **B7** with the amino acid residues surrounding the catalytic cavity of hCES2A.

could form an irreversible covalent bond exclusively with serine nucleophiles of target serine hydrolase(s). To sought the most suitable carbamate moiety, a suite of **B7** carbamates with increasing molecular size was rationally designed and nine of them (**C1**−**C9**) were successfully synthesized for testing anti-hCES2A activity.

As shown in Table 1 and Supporting Information Fig. S6, all synthesized **B7** carbamates displayed significant time-dependent inhibition against hCES2A, indicating these agents acted as covalent inhibitors of this key serine enzyme. Among all tested **B7** carbamates, four **B7** carbamates (**C2**−**C5**) showed extremely potent anti-hCES2A effects, showing the IC_{50} values ranging from 0.56 to 5.44 nmol/L (following 33 min pre-incubation). By contrast, introducing a mono-substituted carbamate (such as **C1**) or a bis-substituted carbamate with relatively bulky group (such as **C8** and **C9**) showed relatively weak anti-hCES2A effects. Following three rounds of screening and structural modifications, the SARs of donepezil-fused derivatives as hCES2A inhibitors are delineated as follows (Fig. 3): (1) Two methoxy groups on the B ring are beneficial for hCES2A inhibition; (2) Introducing a halogen substitution on A ring will diminish the anti-hCES2A activity; (3) Introduction of a hydroxyl group at the C-2 site on A ring significantly enhances hCES2A inhibition; (4) Carbamating the C-2 phenolic group of **B7** markedly bolsters the anti-hCES2A effect, especially for the bis-substituted carbamates with small alkyl groups. The carbamates bearing large substituents

Table 1 Structures, log*P* and IC_{50} values of **B7** carbamates against hCES2A.

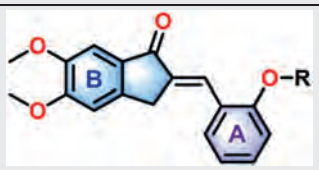

Compound	R	MW	Log*P*	IC_{50} (nmol/L)		Ratio
				3 min	33 min	
B7	OH	296.32	3.06	106 ± 15.5	325 ± 59.5	0.33
C1		353.37	3.03	1183 ± 135.1	346.3 ± 29.13	3.42
C2		367.40	3.27	11.47 ± 2.47	1.74 ± 0.10	6.59
C3		381.43	3.51	3.67 ± 0.23	0.56 ± 0.03	6.55
C4		395.46	3.80	11.76 ± 2.07	3.20 ± 0.38	3.68
C5	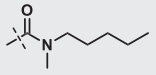	423.51	4.57	25.71 ± 2.68	5.44 ± 0.57	4.73
C6	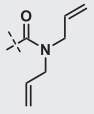	419.48	4.32	350.2 ± 25.38	75.84 ± 4.77	4.62
C7	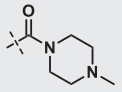	422.48	3.03	258.1 ± 37.77	35.26 ± 3.67	7.32
C8	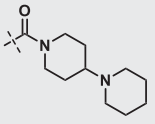	490.60	4.31	732.5 ± 71.69	225.3 ± 13.40	3.25
C9	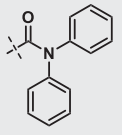	491.54	5.54	901.2 ± 127.4	305.7 ± 26.69	2.95

(such as **C8** and **C9**) will increase steric hindrance, thereby reducing the reaction reactivity and the efficiency of covalent modification.

2.4. *C3 shows potent anti-hCES2A effects in living cells*

Considering that **C2**, **C3**, **C4**, and **C5** displayed potent anti-hCES2A effects, their druglike properties, inactivation kinetics, and inactivation rate constants were further investigated. The physicochemical properties of these four carbamates all complied with Lipinski's rule of five, indicating their potential of high oral bioavailability (Supporting Information Table S4). It was found that these carbamates possessed dose-dependent and time-dependent inactivation profiles of hCES2A (Supporting Information Table S5 and Supporting Information Fig. S7). Especially, **C3** showed a K_I value of 1.58 nmol/L and a K_{inact} value of 0.035 min^{-1} (Fig. 4A and B). As a result, the K_{inact}/K_I value of **C3** (0.022 L/nmol/min) was superior to that of **C2** (0.021 L/nmol/min), **C4** (0.009 L/nmol/min), and **C5** (0.012 L/nmol/min). These findings clearly suggest that **C3** acts as an extremely potent hCES2A inactivator with strong binding affinity and exceptional covalent modification efficiency. Furthermore, the inhibitory effects of **B7** carbamates on intracellular hCES2A were tested in a non-invasive and real-time manner, by utilizing *N*-(2-butyl-1,3-dioxo-2,3-dihydro-1*H*-benzo[*de*]isoquinolin-6-yl)-2-chloroacetamide (NCEN, a hCES2A specific fluorogenic substrate) as a fluorogenic substrate[45]. As shown in Fig. 4C and Supporting Information Fig. S8, **C2**, **C3**, **C4**, and **C5** could dose-dependently attenuate the green signals derived from hCES2A-catalyzed NCEN hydrolysis, confirming the potent intracellular hCES2A inhibition of these carbamates. Specifically, the IC_{50} value of **C3** against intracellular hCES2A was determined as low as 2.35 nmol/L (Fig. 4D), which was slightly potent than **C2** (3.63 nmol/L), **C4** (5.25 nmol/L), and **C5** (6.85 nmol/L). These

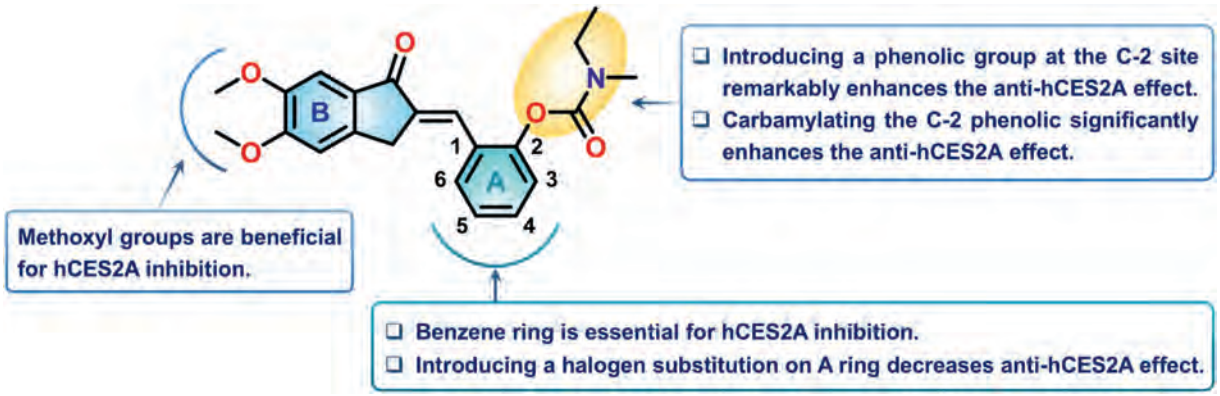

Figure 3 A comprehensive SAR summary of donepezil derivatives as hCES2A inhibitors.

findings motivated further exploration of the inhibitory mechanisms and drug-liker properties of this newly synthetic agent.

2.5. *Inactivation mechanisms of **C3** towards hCES2A*

To validate the inhibition mode of **C3** against hCES2A, the dialysis assays were conducted first. After dialysis to remove the positive inhibitor LPA, the hCES2A activity showed a gradually recovering trend over time (Supporting Information Fig. S9). In sharp contrast, **C3** could completely inhibit hCES2A following 4-h dialysis, indicative of its irreversible inhibition mode (Fig. 4E). After then, the covalent binding sites of **C3** on hCES2A were identified by nano-LC−MS/MS. As expected, the serine residues of hCES2A could be attacked by the carbamate of **C3** to form the carbamate-modified peptides (Scheme 1D). During this process, a mass shift of the carbamate (+85.052764 Da) would be observed from the modified peptide. Following co-incubation with **C3**, both Ser-228 and Ser-236 in the peptide (^{226}GESAGGTSVSSLVVSPISQGLF^{247}) were found to be covalently modified by **C3**, with mass additions of 85.054130 and 85.056379 Da, respectively (Table 2, Fig. 4F, and Supporting Information Fig. S10). The catalytic triad (Ser-228, Glu-345, and His-457) of hCES2A is well-known to be vital for its hydrolytic function[46]. Covalent modification of Ser-228 would completely block the hydrolytic activity of hCES2A, while covalent modification of Ser-236 might also affect the substrate-enzyme binding process. Such selective modifications of two functional serine residues located at the catalytic cavity of hCES2A led to **C3** being an extremely potent hCES2A inactivator.

2.6. *Covalent docking simulations of **C3***

Next, the inactivation mechanisms of **C3** against hCES2A (residue 38−533) were studied by covalent docking simulations. As illustrated in Fig. 4G, **C3** could stably bind to the catalytic cavity of hCES2A *via* alkyl and π−alkyl interactions with several key residues like Phe-106, Leu-461, and Val-464. The catalytic distance between the carbonyl carbon atom of carbamate and the Ser-228 was as low as 4.3 Å. Such a favourable spatial orientation facilitated the hydrolytic metabolism of **C3**. Following hCES2A-catalyzed hydrolysis, the ester bond of **C3** could be hydrolyzed into two fragments, while the carbamate fragment could form a covalent bond with Ser-228 (Fig. 4H). The stability of the unmodified hCES2A and **C3**-modified hCES2A was then analyzed by molecular dynamics simulations. The apo- and **C3**-modified hCES2A reached a state of equilibrium during 100 ns simulations (Supporting Information Fig. S11A). Furthermore, the gyration radius of the carbamate 228- and carbamate 236- hCES2A were averagely maintained between 2.22 and 2.24 nm, while the unmodified protein showed a larger average gyration radius of 2.25 nm Fig. S11B). Meanwhile, RMSF analysis was used to underscore the difference in protein stability at the amino acid level. Notably, the core amino acids at pocket entry (residue 100−115 and 450−470) in **C3**-modified hCES2A showed lower fluctuation coefficients than those in the unmodified hCES2A, suggesting that **C3** modification enhanced protein stability (Fig. S11C). 3D interaction analysis showed that the carbamate moiety bound at Ser-228 created strong hydrogen bond interactions with Gly-231, Thr-232, and Glu-253, while the carbamate moiety bound at Ser-236 formed hydrogen bonds with Thr-232, Ser-233, Ser-235, Val-239, and Ser-240 (Fig. S11D−S11F). These newly created hydrogen bonding interactions make hCES2A more stable *via* bringing the residues closer and promoting a more compact conformation, thereby resulting in a substantial decrease in enzyme activity or even complete inactivation.

2.7. ***C3** strongly blocks irinotecan hydrolysis in intestinal S9*

Prior to the animal test, the potency of **C3** against CES2A-catalyzed irinotecan hydrolysis was investigated in intestinal S9 from both mouse and human. Following 30 min of pre-incubation, **C3** dose-dependently inhibited CES2A-catalyzed irinotecan hydrolysis in mouse intestinal S9, showing an IC_{50} value of 90.35 nmol/L (Fig. 4I). By contrast, **C3** showed more potent anti-CES2A activity in human intestinal S9, demonstrating an IC_{50} value of 32.79 nmol/L (Fig. 4J). These findings clearly demonstrated that **C3** could strongly block irinotecan hydrolysis in the intestinal preparations from both species. Next, the effects of **C3** for mitigating irinotecan-induced intestinal damage in human intestinal organoids were tested. As shown in Fig. 4K, **C3** significantly restored the growth of human intestinal organoids challenged by irinotecan, *via* blocking the formation of SN-38 in human intestinal organoids (Fig. 4L and M). These findings demonstrate that **C3** shows efficient cell-membrane permeability and potent cross-species efficacy against mammalian CES2A, providing a significant basis for mitigating ITGT in complex biological systems.

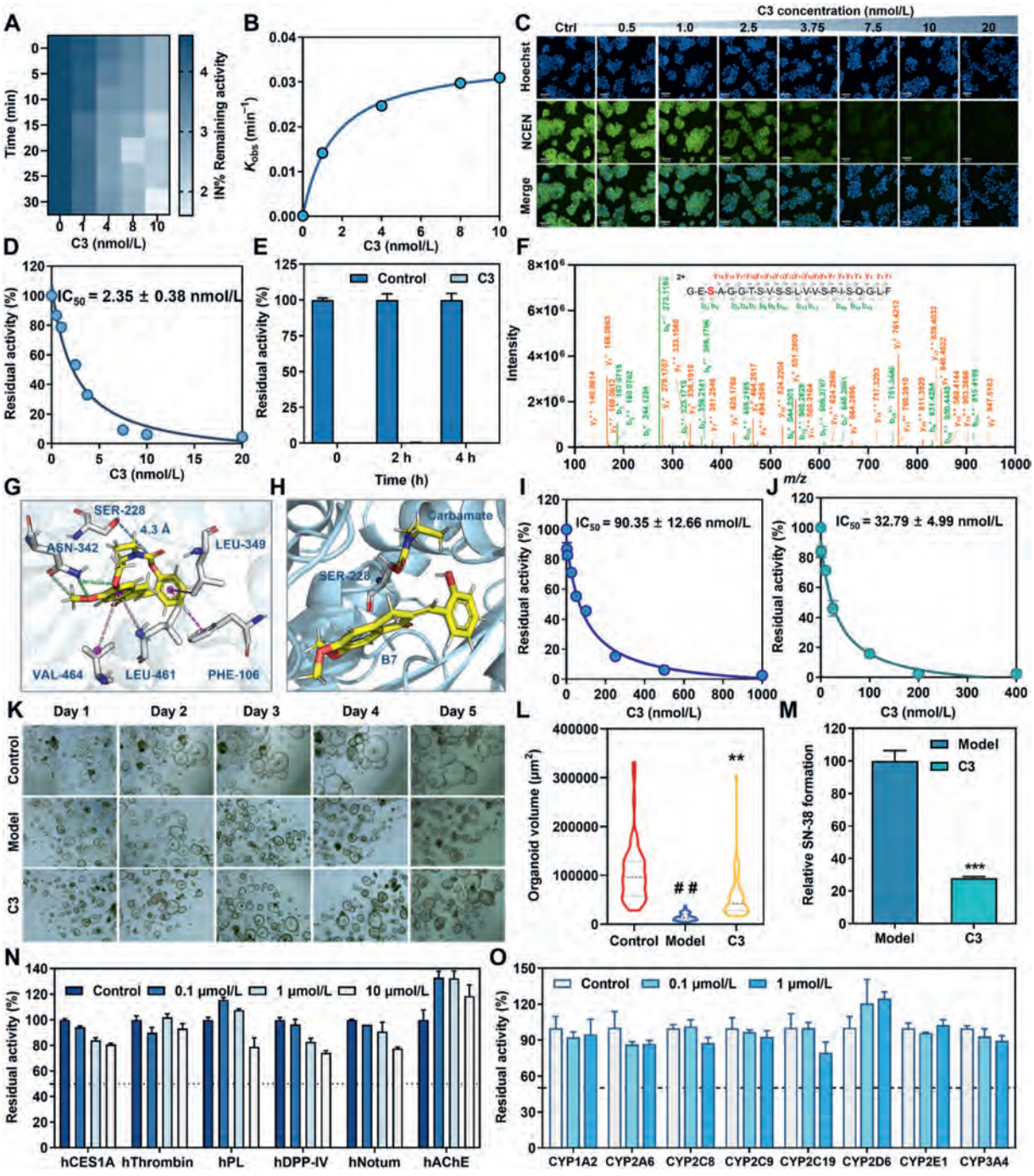

Figure 4 **C3** showed high specificity and potent inhibitory effects against intracellular hCES2A. (A) Inactivation kinetics of **C3** against hCES2A. (B) The hyperbolic plot of K_{obs} of hCES2A against **C3** concentrations. (C) Inhibition of hCES2A in living HepG2 cells with increasing concentrations of **C3**. (D) Dose-dependent inhibition curves of **C3** against intracellular hCES2A. (E) Residual activity of hCES2A after dialysis with/without **C3**. (F) MS^2 spectra of the peptide (GES*AGGTSVSSLVVSPISQGLF) covalently modified by **C3**. (G) The binding mode of **C3** (yellow) docked with hCES2A (blue). (H) Binding mode of the carbamate moiety of **C3** with the catalytic residue (Ser-228) of hCES2A. (I, J) Dose-dependent inhibition curves of **C3** against S9-catalyzed irinotecan hydrolysis from mouse intestine (I) and human intestine (J). (K) **C3** restored the growth of human intestinal organoids challenged by irinotecan. (L) The surface areas of intestinal organoids in each group on Day 5. $^{\#\#}P < 0.01$ *vs.* Control group; $^{**}P < 0.01$ and $^{***}P < 0.001$ *vs.* Model group. (M) **C3** significantly blocks the formation of SN-38 in human intestinal organoids challenged by irinotecan on Day 5. (N) Specificity of **C3** (0.1, 1, and 10 μmol/L, final concentration) against hCES1A, hThrombin, hPL, hDPP-IV, hNotum, and hAChE. (O) The inhibition effects of **C3** on hepatic P450 enzymes.

Table 2 Identification of the covalent binding sites of **C3** on hCES2A by nanoLC−MS/MS.

Peptide	Binding site	$[M+H]^+$ (Da)	Theoretical $[M+H]^+$ (Da)	Peptide coverage	Serine coverage
^{226}GES*AGGTSVSSLVVSPISQGLF^{247}	Ser-228	2164.1145	2164.1132	85.33%	86.84%
^{226}GESAGGTSVSS*LVVSPISQGLF^{247}	Ser-236	2164.1165	2164.1132		

2.8. *C3 shows exceptional selectivity towards hCES2A*

Next, the target specificity of **C3**, chemical stability, as well as its potential for drug-drug interactions were investigated. The similar catalytic features in the serine hydrolase superfamily tend to be an inevitable challenge for the newly developed covalent inhibitors to achieve high specificity toward hCES2A over other human serine hydrolases[28,47]. Herein, the specificity of **C3** towards hCES2A was tested using a suite of important human serine hydrolases, including hCES1A, hNotum, hPL, hThrombin, hDPP-IV, and hAChE (Supporting Information Table S6). As shown in Fig. 4N, **C3** showed excellent specificity towards hCES2A and weakly inhibited other serine hydrolases even at high concentration (10,000 nmol/L), especially hAChE. A comprehensive analysis of the binding conformations of **C3** with hCES1A and hAChE revealed that the metabolic site of the carbamate moiety was far from the catalytic residues of the targets of interest, making it difficult to form a catalytic conformation with metabolic potential (Supporting Information Fig. S12). These findings suggest that **C3** is a specific hCES2A inhibitor with little potential for cross-reactivity with other human serine hydrolases. Furthermore, **C3** presented favourable chemical stability in both phosphate buffered saline (PBS), artificial gastrointestinal fluid, as well as plasma from human and mouse (Supporting Information Figs. S13−S15). **C3** also did not trigger significant inhibitory effects on nine important drug-metabolizing enzymes, including CYP1A2, CYP2A6, CYP2C8, CYP2C9, CYP2C19, CYP2D6, CYP2E1, CYP3A4, and UGT1A1 (Supporting Information Table S7, Fig. 4O, Supporting Information Fig. S16). These findings clearly suggest that **C3** is unlikely to cause adverse drug-drug interactions, with outstanding specificity and chemical stability.

2.9. *C3 shows good safety profiles in mice*

Next, the tolerance of **C3** was tested by the observation of the toxic signs and the changes in body weight in both the **C3**-treated group and the vehicle group (0.5% sodium carboxymethyl cellulose solution, *w*/*v*) in mice. The administration of **C3** at a dose of 250 mg/kg did not result in any observed toxicity, mortality, or morbidity. No alterations were observed in the movement, physical and behavioural parameters, general appearance, salivation, or lacrimation from the day of administration throughout the study period. Additionally, body weight is an important indicator of overall health status. After 14-day successive administration of **C3** (250 mg/kg/day) in mice, there was no notable difference in mean body weight compared to the control group (Fig. 5A). This indicated that long-term exposure to **C3** does not lead to alterations in growth or development. To further investigate potential toxic effects on vital organs, histopathological examinations were conducted on various tissues including heart, liver, lung, spleen, kidney, brain, and gastrointestinal tract from both the **C3**-treated groups and controls (Fig. 5B). No lesions or inflammation were observed in any of these tissues examined under microscopic evaluation. Liver and kidney function tests are important indicators of overall health and can provide valuable information about the functioning of these organs. The fact that there were no alterations in these tests suggested that **C3** was well-tolerated by the body and did not cause any damage or dysfunction to the liver or kidneys (Fig. 5C−J). These results clearly demonstrate that oral administration of **C3** at a high dose (250 mg/kg/day) for 14 consecutive days in mice elicited no observable organ injury or pathological abnormalities, suggesting an excellent safety profile of **C3**.

2.10. *C3 shows favorable tissue distribution in mice*

The tissue distribution of **C3** in mice after gavage administration was investigated for mapping its exposure to different organs. As shown in Supporting Information Fig. S17, after gavage administration of **C3** in mice at a single dose of 100 mg/kg, **C3** could be detected in all tested organs. Interestingly, the high exposure levels of **C3** were found in the duodenum, jejunum, ileum, and colon. In contrast to its high exposure levels in the intestinal system, extremely low exposure levels of **C3** were detected in serum and other deep organs (such as the heart, liver, spleen, lung, and kidney) in mice. These observations unambiguously suggest that **C3** shows favourable tissue distribution (high exposure to the intestinal system but extremely low exposure to serum and deep-organs) following oral administration, which partially explain the high safety profiles of this agent and indicate that this agent can efficiently exert its anti-CES2A effects in the gut tract *via* targeting intestinal CES2A. Following a single oral administration of **C3** (100 mg/kg), the plasma concentration-time curves were plotted (Supporting Information Table S8 and Fig. S18). The peak plasma concentration (C_{max} = 349.9 ng/mL) was observed at approximately 7.6 h, while the metabolic half-life ($t_{1/2}$) was determined as 5.07 h. These findings suggest that **C3** can be slowly absorbed into circulating system, and showed acceptable metabolic half-life *in vivo*.

2.11. *C3 significantly ameliorates ITGT in tumor-bearing mice*

Inspired by the above findings, the ameliorative effects of **C3** on ITGT were investigated in tumor-bearing mice. As depicted in Fig. 6A, irinotecan could cause severe gut toxicity in colorectal tumor-bearing mice, evidenced by the decreased body weight, shortened colonic length, and increased DAI scores ($P < 0.05$) (Fig. 6B−E, Supporting Information Fig. S19). In sharp contrast, the gut toxicity of mice was conspicuously alleviated after treatment with **C3**, as evidenced by the decreased DAI score, the increased body weight and lengthened colonic length ($P < 0.05$). Interestingly, the ameliorative effects of **C3** were much better than those of the positive drug (LPA, 10 mg/kg). These observations preliminarily suggest that **C3** efficiently ameliorates the gut toxicity induced by irinotecan. The histomorphology changes of colon tissues were also carefully examined. Compared to control

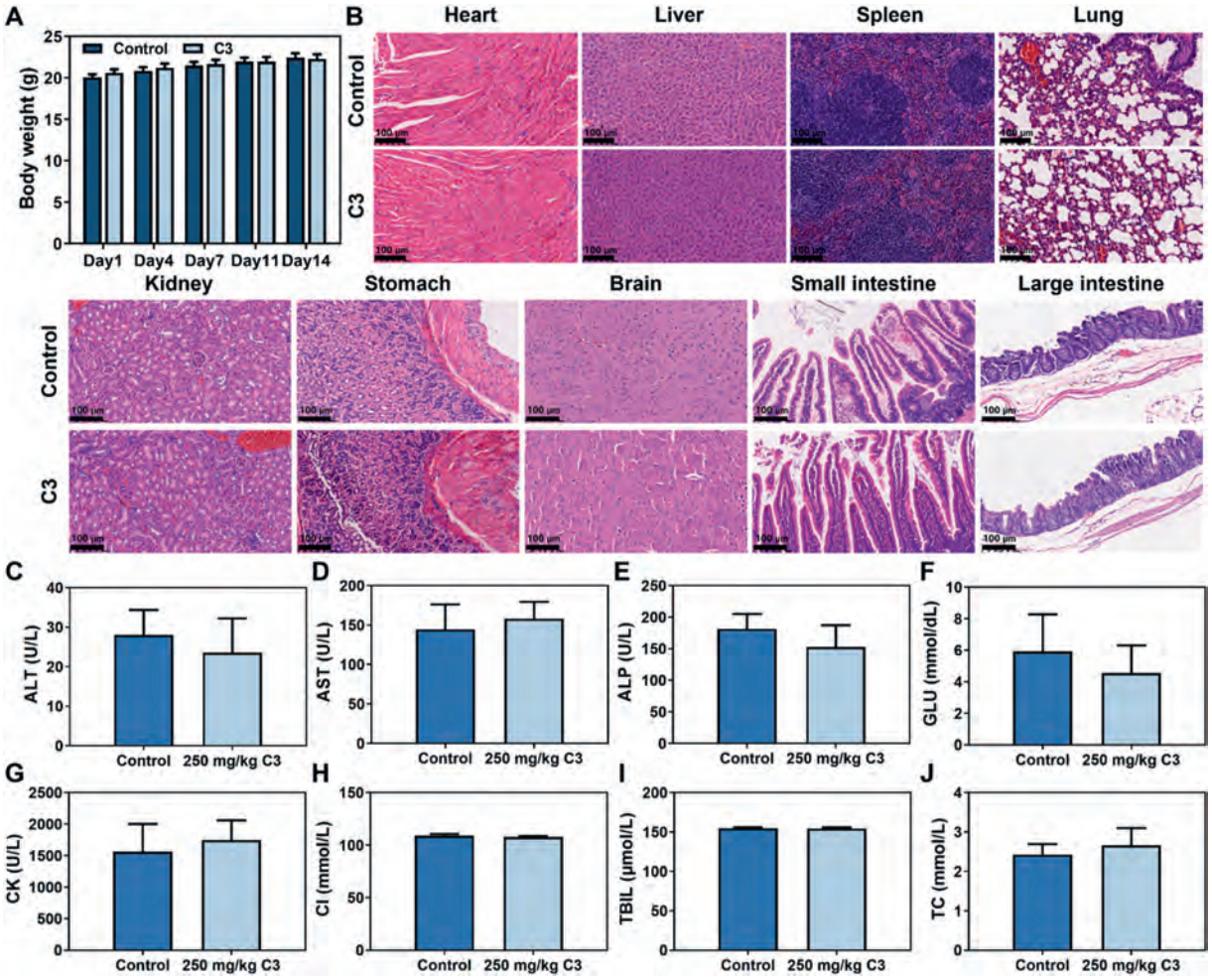

Figure 5 **C3** shows good safety profiles in mice. (A) Body weight changes of mice after gavage administration of 250 mg/kg **C3** ($n = 10$). (B) Histopathological studies of the mouse organs following oral administration of **C3** (250 mg/kg) for 14 consecutive days. Scale bar = 100 μm. (C−J) The serum biochemical parameters of control and **C3**-treated mice. (C) Glutamic-pyruvic transaminase (ALT); (D) Glutamic-oxalacetic transaminase (AST); (E) Alkaline phosphatase (ALP); (F) Glucose (GLU); (G) Creatine kinase (CK); (H) Calcium ion (CI); (I) Total bilirubin (TBIL); (J) Total cholesterol (TC). The above results were expressed as mean ± SD, $n = 10$.

group, the villi, crypts, goblet cells were significantly depleted, accompanied by abundant inflammatory cell infiltration in irinotecan-treated mice. However, the colon tissue structure in the **C3** group (25 and 50 mg/kg) was relatively intact (Fig. 6F). These findings unambiguously demonstrate that irinotecan seriously damages the colon tissue, while **C3** can effectively reverse the morphological damage of irinotecan-challenged colon tissues.

Subsequently, the inflammatory factors in colon tissue were measured. Compared to control group, the levels of IL-6, IL-1β, and TNF-α were elevated observably in irinotecan-treated mice ($P < 0.01$), while this trend could be reversed by **C3** (25 and 50 mg/kg) and LPA (10 mg/kg) to different extents ($P < 0.05$) (Fig. 6G−I). These findings clearly demonstrate that **C3** has potent anti-inflammatory effects in protecting the colon from inflammatory damage. The gut barrier integrity was also examined by determining the expression levels of the tight junction proteins (including ZO-1, Claudin-1, and Occludin). Immunofluorescence staining assays showed that all tested tight junction proteins were up-regulated remarkably in **C3** (25 and 50 mg/kg) treated mice (Fig. 6J, Supporting Information Fig. S20). These findings validate that **C3** can reinforce the intestinal epithelial function and intestinal barrier. We also measured the exposure levels of SN-38 in colon tissues from different groups. As expected, **C3** dramatically decreased the exposure level of SN-38 in mice colon ($P < 0.01$) (Fig. 6K). This phenomenon prompted us to further investigate the underlying cause of decreased SN-38 exposure in colonic tissue. Considering that UGT1A1 in intestinal system plays a crucial role in catalyzing SN-38-*O*-glucuronidation to form SN-38G, we investigated the impact of **C3** on UGT1A1 expression in colonic tissue. It was found that **C3** significantly up-regulated the expression of UGT1A1 in ITGT mice, particularly at the high dose ($P < 0.01$) (Supporting Information Fig. S21). Furthermore, upon addition of **C3**, the intestinal CES2A was inhibited completely, which strongly block the formation of SN-38 from irinotecan. Given that irinotecan could also trigger hepatotoxicity and nephrotoxicity in clinical, we also tested the serum levels of ALT, AST, UREA and CREA in different groups. The results show that irinotecan significantly elevated the serum levels of

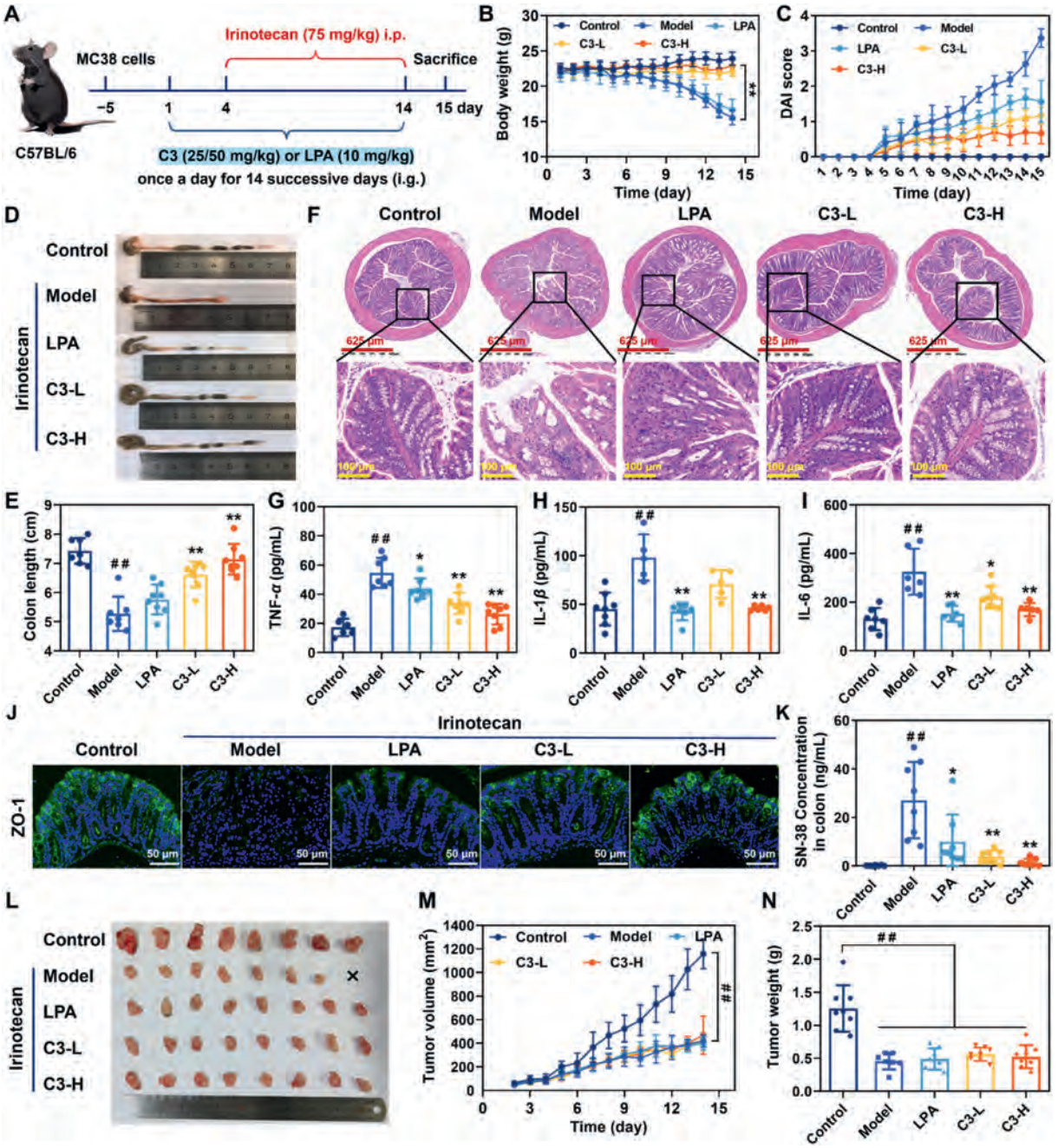

Figure 6 **C3** significantly alleviates ITGT in tumor-bearing mice. (A) Experimental design for **C3** treatment on ITGT in tumor-bearing mice. (B−E) Body weight (B) DAI scores (C), colon images (D), colon length (E) of the mice among different groups. (F) H&E staining of mice colons. (G−I) The levels of inflammatory factors including TNF-α (G), IL-1β (H), and IL-6 (I) in mice colons from different groups. (J) Immunofluorescence staining for tight junction proteins (ZO-1) of mice colons, scale bar: 50 μm. (K) The exposure levels of SN-38 in mice colons from different groups. (L−N) The tumor images (L), tumor volume (M), and tumor weight (N). The data were expressed as mean ± SD, $^{\#\#}P < 0.01$ *vs.* Control group; $^{*}P < 0.05$ and $^{**}P < 0.01$ *vs.* Model group, $n = 5$−8. LPA was used as a positive drug.

ALT, AST, UREA and CREA in mice ($P < 0.01$), but **C3** (25 and 50 mg/kg) could markedly reverse these abnormal signs ($P < 0.05$) (Supporting Information Fig. S22). These observations strongly suggest that **C3** can ameliorate irinotecan-induced multiple organ injuries. More importantly, **C3** did not affect the *in vivo* anti-tumor effects of irinotecan, no significant difference in both tumor volume and tumor weight was observed between irinotecan treatment group and **C3**-irinotecan co-treatment groups (Fig. 6L−N). All these *in vivo* findings strongly suggest that **C3** can significantly ameliorate ITGT but do not diminish the anti-tumor effects of irinotecan in tumor-bearing mice.

3. Conclusions

In summary, several orally active, and serine-targeting covalent hCES2A inhibitors were developed following three rounds of SBDD

and SAR studies. In the 1st round of hit selection, a novel donepezil derivative (**A3**) was identified as a hit compound with a relatively strong anti-hCES2A effect (IC_{50} = 0.92 μmol/L). In the 2nd round of lead discovery, a strong reversible hCES2A inhibitor (**B7**, IC_{50} = 0.11 μmol/L) was gained following SBDD and SAR analysis. Given that the C-2 phenolic group of **B7** formed a hydrogen bond with the catalytic residue (Ser-228) of hCES2A, a suite of **B7** carbamates were developed as hCES2A covalent inhibitors. A comprehensive SAR studies showed that carbamating the C-2 phenolic group of **B7** markedly enhanced the anti-hCES2A effect, especially for the carbamates with small alkyl groups. Among all tested carbamates, **C3** showed the most potent anti-hCES2A activity in a time-dependent manner (IC_{50} = 0.56 nmol/L following 33 min pre-incubation) *via* covalent modifying two key serine residues (Ser-228 and Ser-236) located at the catalytic cavity of hCES2A. *In vivo* tests showed that **C3** possessed favourable safety profiles and high intestinal exposure following gavage administration, as well as impressive therapeutic effects for ameliorating ITGT in tumor-bearing mice. Collectively, this study showcases a rational strategy for developing drug-like and serine-targeting covalent inhibitors against target serine hydrolase(s), while **C3** emerges as an orally active hCES2A inhibitor for ameliorating ITGT or modulating the treatment outcomes of hCES2A substrates.

4. Experimental

4.1. Chemistry

All commercially available reagents were used without further purification. The reaction was monitored by TLC on glass-packed precoated silica gel plates from Qingdao Haiyang Chemical Co., Ltd. (China), and visualized with an UV lamp. The crude was purified by column chromatography using silica gel (230−400 mesh) purchased from Qingdao Haiyang Chemical Co., Ltd. (China). The purity of target compounds was confirmed by high-performance liquid chromatography (HPLC) analysis to be over 96%. HPLC analysis was carried out on a Waters600-2487 plus system with the use of a Kromasil C18 column (4.6 mm × 250 mm, 5 μm). ^{1}H NMR and ^{13}C NMR spectra were recorded on a Varian INOVA spectrometer, using TMS as an internal standard in $CDCl_3$ or DMSO-d_6 at 400 and 100 MHz, respectively. MS spectra data were obtained on an Agilent-6210 TOF LC−MS spectrometer. More information regarding the chemical synthesis and structural characterization was provided in Supporting Information Schemes S1−S3 and Supporting Information Figs. S23−S60).

4.2. Inactivation kinetic analysis of *C3*

Inactivation kinetic analysis was carried out according to the previous reported method[48]. A round of different **C2, C3, C4** and **C5** concentrations was selected for incubation for different periods. After different preincubation time, the reaction was initiated by adding the substrate fluorescein diacetate (FD). The natural logarithm of the residual hCES2A activity was plotted against the preincubation time.

4.3. Identification of the covalent binding sites of *C3* on hCES2A

The **C3**-modified peptides were analyzed using nanoLC−MS/MS[49,50]. Firstly, the purified hCES2A (150 μg, final content) was co-incubated with the small molecule inhibitor **C3** (10 μmol/L, final concentration) at 37 °C for 4 h. Then to finish the process of protein denaturation, reduction, and alkylation, the mixtures were separately treated with urea, dithiothreitol, and iodoacetamide. The enriched proteins were subsequently digested by trypsin at 37 °C for 16 h after being solubilized with NH_4HCO_3 solution (pH 8.0, 50 mmol/L) containing 5% acetonitrile (*v*/*v*). The resulting peptides were desalted on a MonoSpin C18 column (GL Sciences Inc.). After the eluents were dried, it was redissolved with 20 μL 0.1% FA (*v*/*v*) for test. The samples were analyzed by the nano-LC−MS/MS system according to the previously reported method[48]. The RAW files obtained from Orbitrap MS were searched for Protein Discovery 2.4 (Thermo Scientific) by using the Sequest HT algorithm, converted to mgf. format by MSconvert and outputted by pLabel v2.4.1.

4.4. Molecular docking simulations

The mature form of hCES2A (Uniprot: O00748) derived from the Alphafold structure was obtained by truncating it at position 26 (Δ26)[51]. AutoDock 1.5.7 was employed to process the truncated hCES2A and **C3**, including removing non-hydrogen bonds and calculating charges. Subsequently, **C3** was docked into the catalytic site of the truncated hCES2A. Enzyme-inhibitor interactions were analysed by Discovery Studio Visualizer 2019.

4.5. Covalent docking simulations

Covalent docking of **C3** with hCES2A was performed by MOE. The optimal conformation was selected as the receptor after ensemble docking. Firstly, the QuickPrep panel was used to pretreat receptor, including structural problem correction, protonation, non-covalent water deletion, and energy optimization. Then, the covalent reaction equation of the **C3** with serine was simulated by MarvinSketch. Finally, the catalytic site Ser-228 was selected as the reaction site and the docking process was run through the covalent docking module.

4.6. Molecular dynamics simulations

Molecular dynamics (MD) simulations for the carbamate-modified hCES2A (residue 38−533) docked with/without **C3** were performed, while the force field for the non-standard amino acid (Ser-228 and Ser-236 carbamate) was generated using AmberTools20 (AMBER 2020, University of California, San Francisco, CA, USA). First, AM1-BCC charges were calculated for the carbamate-modified hCES2A at serine. The atoms, bonds, angles, and dihedral parameters were then determined using the amber99sb-ildn force field and verified with parmchk2. Coordinate and topology files were generated using the leap program and converted to GROMACS topology files *via* ACYPE. Finally, manually created residue topology (rtp) and hydrogen database (hdb) files were added to the amber99sb-ildn force field library. The apo-hCES2A and carbamate-modified hCES2A were prepared for MD simulations. Energy minimization was performed using 50,000 steps of the steepest descent method. The free hCES2A and carbamate-modified hCES2A (carbamate-hCES2A adduct) were solvated using the TIP3P water model, with sodium ions added to neutralize the charges. The system was equilibrated with 100 ps of NVT heating to 310 K, followed by 100 ps of NPT equilibration. Finally, MD simulations were conducted in 0.15 mol/L NaCl at 310 K (V-rescale thermostat) under 1 bar of

pressure (Parrinello−Rahman barostat) for 100,000 ps. After then, 3D-interaction analysis was performed by clustering equilibrium conformations and selecting the most representative structure, which was visualized using Discovery Studio Visualizer (BIOVIA Discovery Studio 2019, Dassault Systèmes, San Diego, CA, USA).

4.7. Inhibition of hCES2A in living HepG2 cells

HepG2 cells were cultivated in an incubator with 5% CO_2 at 37 °C using Dulbecco's modified Eagle's medium (DMEM) supplemented with 10% FBS (*v*/*v*) and 1% P/S (*v*/*v*). Then, HepG2 cells were seeded into 96-well black-clear plates at a density of 20,000 cells per well. After overnight incubation, the culture medium was discarded, and different concentrations of **C2**, **C3**, **C4** and **C5** were diluted with the culture medium and added to the plate at 100 μL per well. The cell culture system was incubated at 37 °C for 1 h, followed by the addition of 100 μL medium containing dyes (NCEN, Hoechst 33342). The final concentrations of NCEN, Hoechst 33342 were 10 μmol/L and 5 μg/mL respectively[45]. After another 45 min, the stained cells were imaged using the Operetta CLS™ High-Content Analysis System (PerkinElmer) for visualization.

4.8. Tolerance trial of *C3*

The healthy mice were randomly split into two groups ($n = 10$, 5 females and 5 males) and intragastrical administrated with **C3** (250 mg/kg, dissolved in 0.5% sodium carboxymethyl cellulose (*v*/*v*) solution) or vehicle (0.5% sodium carboxymethyl cellulose solution, *v*/*v*) for 14 consecutive days. The behavioural pattern, and physical appearance, in addition to other adverse effects were monitored timely. The body weight, food intake, and water consumption were meticulously recorded. On the 14th day of the experiment, organ weights including heart, liver, brain, lungs, kidney, and spleen were carefully dissected and weighed. Hematological and biochemical analysis were performed on collected blood samples. The tissues were fixed in 10% formalin solution and then embedded in paraffin wax after the samples were dehydrated in graded alcohol. Subsequent staining was performed using hematoxylin−eosin (H&E). The dissected organs underwent histopathological examination under light microscopy.

4.9. Tissue distribution of *C3* in mice

Ten mice were randomly divided into two groups. For one week, all mice were kept in cages under controlled environmental factors with free access to food and water. **C3** (100 mg/kg) was intragastrical administrated, then eighteen mice were anesthetized by pentobarbital after administrating 0.5 and 1 h, respectively. The tissues were quickly removed, and blood samples were taken from the abdominal aorta. After then, the blood samples were centrifuged at 5929×*g*, 4 °C for 10 min, and the supernatant was stored at −80 °C.

The blood samples of 30 μL were added with 90 μL in acetonitrile (30 ng/mL lansoprazole as internal standard). Then the samples were centrifuged at 12,000 rpm at 4 °C for 15 min, and the supernatant was taken for test. The samples of each tissue were homogenized and accurately weighed before being added 300 μL PBS (pH 7.4) and magnetic beads. All weighed tissue were ground by the tissue grinder and the homogenate was centrifuged at 9000×*g*, 4 °C for 20 min. After that, a BCA Protein Quantification Kit was used to measure the protein concentration in the supernatant, and 25 μL tissue supernatant was added into 125 μL LC grade acetonitrile. After centrifuging at 20,000×*g* for 30 min at 4 °C, the protein was precipitated. Following that, the concentrations of **C3** were calculated using UHPLC−Q-Orbitrap HRMS analysis.

4.10. Construction of irinotecan-induced gut toxicity in tumor-bearing mice

Forty male C57BL/6J mice (6−8 weeks old, weighing 18−20 g) were bought from the laboratory animal centre, Shanghai University of Traditional Chinese Medicine (Certificate of Conformity: No. SYXK, 2022-0009). The experiments were approved by Shanghai University of Traditional Chinese Medicine Animal Care and Ethics Committee (PZSHUTCM2311130003). The animals were acclimatized to laboratory conditions (23 °C, 12 h/12 h light/dark, 50% humidity, ad libitum access to food and water) for 1 week before experiments. The ITGT models were established in tumor-bearing mice based on a previous study[52]. Briefly, 1×10^6 cells were subcutaneously injected into the right flank of mice. When the tumor reached approximately 50 mm^3 (approximately 5 days), the mice were randomly divided into 5 groups with 8 mice in each group. The mice were intraperitoneally injected with a 75 mg/kg dose of irinotecan hydrochloride (Yuanye Bio-Technology Co., Ltd., Shanghai) for 10 consecutive days to establish diarrheal model from Days 4 to 14. LPA (10 mg/kg body weight, positive drug), **C3-L** (25 mg/kg body weight) and **C3-H** (50 mg/kg body weight) were intragastric administration (*p.o.*) for 14 consecutive days.

The body weight, stool consistency and tumor volume were recorded daily. The disease activity index (DAI) score was used to comprehensively evaluate the daily assessment data for body weight, stool consistency, and colonic gross bleeding range based on previous descriptions[53]. After mice were sacrificed, the blood was collected for biochemical analysis, the colon tissues were rapidly isolated from the proximal rectum, freed of adherent tissues, and rinsed with phosphate buffer saline. Colon biopsy specimens of 1 cm-length were fixed with 4% paraformaldehyde for H&E staining and immunofluorescence of tight junction protein (ZO-1, Claudin-1 and Occludin). The residual colon tissue was stored at −80 °C for further analysis.

4.11. Quantification of SN-38 in colon tissues of tumor-bearing mice

The colon tissue, weighing precisely 20 mg, was finely minced, and then homogenized in 200 μL PBS while maintaining an ice bath for a duration of 2 min. The supernatant was collected and subsequently subjected to centrifugation at 12,000×*g* for 15 min at 4 °C. A fivefold excess of ice-cold acetonitrile containing lansoprazole (the internal standard) was added to the supernatant and vigorously mixed. Subsequently, samples were centrifuged at 20,000×*g* for 30 min at 4 °C. Following centrifugation, a volume of 2 μL from the resulting supernatant was injected into the UPLC−MS/MS system for subsequent analysis. Quantification was performed in the positive ion mode using the following methods: SN-38 was detected at *m*/*z* 393.2 → 349.2, with a collision energy (CE) value of 35 eV. Lansoprazole was detected at *m*/*z* 370.1 → 252.0, with a CE value of 17 eV. Quantification of SN-38 was determined by calculating the ratio of the peak area

of each sample to that of the internal standard. Standard curves (0−1000 ng/mL) of SN-38 were constructed using MultiQuantTM software (SCIEX).

4.12. Statistical analysis

All statistical analysis was determined by GraphPad Prism 9.5 (GraphPad Software, Inc., La Jolla, USA). Data were compared between three or more groups using one-way ANOVA and between two groups using Student's *t*-test. Data are expressed as the mean ± standard deviation (SD). Graphical Abstract was depicted by FigDraw.

Acknowledgments

This work was financially supported by the National Natural Science Foundation of China (Nos. 82104281, 82273897, and 22367007), China Postdoctoral Science Foundation (Nos. 2022M712153, and 2023M742380), The Fundamental Research Funds for Hainan University (KYQD(ZR)23002, China), Hainan Provincial Natural Science Foundation of China (824RC500), and PhD Program in Key Fields at Shanghai University of Traditional Chinese Medicine (GJ2023004, China), Liaoning Province Science and Technology Plan Alliance Fund project (2024-BSLH-041, China). The authors also thank Professor Guanghui Zhu from the Shanghai Municipal Hospital of Traditional Chinese Medicine, for providing human intestinal tissues for constructing human intestinal organoids (2024SHL-KYYS-63, China).

Author contributions

Guangbo Ge, Dapeng Chen, Zhipei Sang conceived and designed the overall study; Ya Zhang, Hairong Zeng, Guanghao Zhu, Xinjuan Li, Changhai Luan, Xinrui Guo, Jian Huang, Dongning Kang, Lu Chen and Zhaobin Guo performed the experiments; Guangbo Ge, Zhipei Sang, Hairong Zeng, Yunqing Song, Ya Zhang, Yufan Fan, Guanghao Zhu and Xinjuan Li analyzed the data; Guangbo Ge, Zhipei Sang, Dapeng Chen, Hairong Zeng, Yunqing Song, Ya Zhang and Yufan Fan wrote the manuscript. Zhangping Xiao provided constructive suggestions for this study. All authors reviewed and approved the final version of the manuscript.

Conflicts of interest

The authors declare no conflict of interest.

Appendix A. Supporting information

Supporting information to this article can be found online at https://doi.org/10.1016/j.apsb.2025.08.007.

References

1. Sanghani SP, Sanghani PC, Schiel MA, Bosron WF. Human carboxylesterases: an update on CES1, CES2 and CES3. *Protein Pept Lett* 2009;**16**:1207−14.
2. Lian J, Nelson R, Lehner R. Carboxylesterases in lipid metabolism: from mouse to human. *Protein Cell* 2018;**9**:178−95.
3. Di L. The impact of carboxylesterases in drug metabolism and pharmacokinetics. *Curr Drug Metabol* 2019;**20**:91−102.
4. Zhang W, Xu G, McLeod HL. Comprehensive evaluation of carboxylesterase-2 expression in normal human tissues using tissue array analysis. *Appl Immunohistochem Mol Morphol* 2002;**10**: 374−80.
5. Jones RD, Taylor AM, Tong EY, Repa JJ. Carboxylesterases are uniquely expressed among tissues and regulated by nuclear hormone receptors in the mouse. *Drug Metab Dispos* 2013;**41**:40−9.
6. Satoh T, Taylor P, Bosron WF, Sanghani SP, Hosokawa M, La Du BN. Current progress on esterases: from molecular structure to function. *Drug Metab Dispos* 2002;**30**:488−93.
7. Lan L, Ren X, Yang J, Liu D, Zhang C. Detection techniques of carboxylesterase activity: an update review. *Bioorg Chem* 2020;**94**: 103388.
8. Konishi K, Fukami T, Ogiso T, Nakajima M. *In vitro* approach to elucidate the relevance of carboxylesterase 2 and *N*-acetyltransferase 2 to flupirtine-induced liver injury. *Biochem Pharmacol* 2018;**155**: 242−51.
9. Sun Z, Wu Y, Liu S, Hu S, Zhao B, Li P, et al. Effects of *Panax notoginseng* saponins on esterases responsible for aspirin hydrolysis *in vitro*. *Int J Mol Sci* 2018;**19**:3144.
10. Jia YM, Ge PX, Zhou H, Ji JZ, Tai T, Gu TT, et al. Vicagrel enhances aspirin-induced inhibition of both platelet aggregation and thrombus formation in rodents due to its decreased metabolic inactivation. *Biomed Pharmacother* 2019;**115**:108906.
11. McQuade RM, Stojanovska V, Donald EL, Rahman AA, Campelj DG, Abalo R, et al. Irinotecan-induced gastrointestinal dysfunction is associated with enteric neuropathy, but increased numbers of cholinergic myenteric neurons. *Front Physiol* 2017;**8**:391.
12. Gao Y, Li W, Chen J, Wang X, Lv Y, Huang Y, et al. Pharmacometabolomic prediction of individual differences of gastrointestinal toxicity complicating myelosuppression in rats induced by irinotecan. *Acta Pharm Sin B* 2019;**9**:157−66.
13. Okunaka M, Kano D, Matsui R, Kawasaki T, Uesawa Y. Evaluation of the expression profile of irinotecan-induced diarrhea in patients with colorectal cancer. *Pharmaceuticals* 2021;**14**:681.
14. Barbounis V, Koumakis G, Vassilomanolakis M, Demiri M, Efremidis AP. Control of irinotecan-induced diarrhea by octreotide after loperamide failure. *Support Care Cancer* 2001;**9**:258−60.
15. Wu PE, Juurlink DN. Loperamide cardiac toxicity: pathophysiology, presentation, and management. *Can J Cardiol* 2022;**38**:1378−83.
16. Wadkins RM, Hyatt JL, Yoon KJ, Morton CL, Lee RE, Damodaran K, et al. Discovery of novel selective inhibitors of human intestinal carboxylesterase for the amelioration of irinotecan-induced diarrhea: synthesis, quantitative structure−activity relationship analysis, and biological activity. *Mol Pharmacol* 2004;**65**:1336−43.
17. Wang DD, Zou LW, Jin Q, Hou J, Ge GB, Yang L. Recent progress in the discovery of natural inhibitors against human carboxylesterases. *Fitoterapia* 2017;**117**:84−95.
18. Song SS, Sun CP, Zhou JJ, Chu L. Flavonoids as human carboxylesterase 2 inhibitors: inhibition potentials and molecular docking simulations. *Int J Biol Macromol* 2019;**131**:201−8.
19. Yi J, Bai R, An Y, Liu TT, Liang JH, Tian XG, et al. A natural inhibitor from *Alisma orientale* against human carboxylesterase 2: kinetics, circular dichroism spectroscopic analysis, and docking simulation. *Int J Biol Macromol* 2019;**133**:184−9.
20. Sun CP, Yang ZJ, Zhao WY, Zhang RY, Li H, Chen LX. A novel 15-spiro diterpenoid dimer from *Andrographis paniculata* with inhibitory potential against human carboxylesterase 2. *Bioorg Chem* 2020;**97**: 103680.
21. Zhao YS, Qian XK, Guan XQ, Song PF, Song YQ, He RJ, et al. Discovery of natural alkaloids as potent and selective inhibitors against human carboxylesterase 2. *Bioorg Chem* 2020;**105**:104367.
22. Huo PC, Guan XQ, Liu P, Song YQ, Sun MR, He RJ, et al. Design, synthesis and biological evaluation of indanone-chalcone hybrids as potent and selective hCES2A inhibitors. *Eur J Med Chem* 2021;**209**: 112856.
23. Wadkins RM, Hyatt JL, Wei X, Yoon KJP, Wierdl M, Edwards CC, et al. Identification and characterization of novel benzil

(diphenylethane-1,2-dione) analogues as inhibitors of mammalian carboxylesterases. *J Med Chem* 2005;**48**:2906−15.
24. Li JN, Cao YF, He RR, Ge GB, Guo B, Wu JJ. Evidence for shikonin acting as an active inhibitor of human carboxylesterases 2: implications for herb-drug combination. *Phytother Res* 2018;**32**: 1311−9.
25. Liu YZ, Pan LH, Bai Y, Yang K, Dong PP, Fang ZZ. Per- and polyfluoroalkyl substances exert strong inhibition towards human carboxylesterases. *Environ Pollut* 2020;**263**:114463.
26. Shi CC, Song YQ, He RJ, Guan XQ, Song LL, Chen ST, et al. Rapalogues as hCES2A inhibitors: *in vitro* and *in silico* investigations. *Eur J Drug Metab Pharmacokinet* 2021;**46**:129−39.
27. Boike L, Henning NJ, Nomura DK. Advances in covalent drug discovery. *Nat Rev Drug Discov* 2022;**21**:881−98.
28. Zheng L, Li Y, Wu D, Xiao H, Zheng S, Wang G, et al. Development of covalent inhibitors: principle, design, and application in cancer. *MedComm* 2023;**2**:e56.
29. Crow JA, Bittles V, Herring KL, Borazjani A, Potter PM, Ross MK. Inhibition of recombinant human carboxylesterase 1 and 2 and monoacylglycerol lipase by chlorpyrifos oxon, paraoxon and methyl paraoxon. *Toxicol Appl Pharmacol* 2012;**258**:145−50.
30. Wheelock CE, Severson TF, Hammock BD. Synthesis of new carboxylesterase inhibitors and evaluation of potency and water solubility. *Chem Res Toxicol* 2001;**14**:1563−72.
31. Hicks LD, Hyatt JL, Stoddard S, Tsurkan L, Edwards CC, Wadkins RM, et al. Improved, selective, human intestinal carboxylesterase inhibitors designed to modulate 7-ethyl-10-[4-(1-piperidino)-1-piperidino]carbonyloxycamptothecin (Irinotecan; CPT-11) toxicity. *J Med Chem* 2009;**52**:3742−52.
32. Zou LW, Jin Q, Wang DD, Qian QK, Hao DC, Ge GB, et al. Carboxylesterase inhibitors: an update. *Curr Med Chem* 2018;**25**:1627−49.
33. Chen X, Mu X, Ding L, Wang X, Mao F, Wei J, et al. Trilogy of drug repurposing for developing cancer and chemotherapy-induced heart failure co-therapy agent. *Acta Pharm Sin B* 2024;**14**:729−50.
34. Sindt F, Seyller A, Eguida M, Rognan D. Protein structure-based organic chemistry-driven ligand design from ultralarge chemical spaces. *ACS Cent Sci* 2024;**10**:615−27.
35. Xu Y, Zhang C, Jiang K, Yang X, Chen F, Cheng Z, et al. Structural repurposing of SGLT2 inhibitor empagliflozin for strengthening anti-heart failure activity with lower glycosuria. *Acta Pharm Sin B* 2023; **13**:1671−85.
36. Pushpakom S, Iorio F, Eyers PA, Escott KJ, Hopper S, Wells A, et al. Drug repurposing: progress, challenges and recommendations. *Nat Rev Drug Discov* 2018;**18**:41−58.
37. Bhutani P, Joshi G, Raja N, Bachhav N, Rajanna PK, Bhutani H, et al. U.S. FDA approved drugs from 2015-June 2020: a perspective. *J Med Chem* 2021;**64**:2339−81.
38. Michino M, Beautrait A, Boyles NA, Nadupalli A, Dementiev A, Sun S, et al. Shape-based virtual screening of a billion-compound library identifies mycobacterial lipoamide dehydrogenase inhibitors. *ACS Bio Med Chem Au* 2023;**3**:507−15.
39. Gehringer M, Laufer SA. Emerging and re-emerging warheads for targeted covalent inhibitors: applications in medicinal chemistry and chemical biology. *J Med Chem* 2019;**62**:5673−724.
40. Singh J, Petter RC, Baillie TA, Whitty A. The resurgence of covalent drugs. *Nat Rev Drug Discov* 2011;**10**:307−17.
41. Bachovchin DA, Ji T, Li W, Simon GM, Blankman JL, Adibekian A, et al. Superfamily-wide portrait of serine hydrolase inhibition achieved by library-versus-library screening. *Proc Natl Acad Sci U S A* 2010;**107**:20941−6.
42. Fan Y, Zhang T, Song Y, Sang Z, Zeng H, Liu P, et al. Rationally engineered hCES2A near-infrared fluorogenic substrate for functional imaging and high-throughput inhibitor screening. *Anal Chem* 2023;**95**: 15665−72.
43. Chang JW, Cognetta 3rd AB, Niphakis MJ, Cravatt BF. Proteome-wide reactivity profiling identifies diverse carbamate chemotypes tuned for serine hydrolase inhibition. *ACS Chem Biol* 2013;**8**: 1590−9.
44. Ghosh AK, Brindisi M. Organic carbamates in drug design and medicinal chemistry. *J Med Chem* 2015;**58**:2895−940.
45. Xue L, Qian X, Jin Q, Zhu Y, Wang X, Wang D, et al. Construction and application of a high-content analysis for identifying human carboxylesterase 2 inhibitors in living cell system. *Anal Bioanal Chem* 2020;**412**:2645−54.
46. Wang D, Zou L, Jin Q, Hou J, Ge G, Yang L. Human carboxylesterases: a comprehensive review. *Acta Pharm Sin B* 2018;**8**:699−712.
47. Pettinger J, Jones K, Cheeseman MD. Lysine-targeting covalent inhibitors. *Angew Chem Int Ed Engl* 2017;**56**:15200−9.
48. Xiong Y, Zhu GH, Zhang YN, Hu Q, Wang HN, Yu HN, et al. Flavonoids in *Ampelopsis grossedentata* as covalent inhibitors of SARS-CoV-2 3CL(pro): inhibition potentials, covalent binding sites and inhibitory mechanisms. *Int J Biol Macromol* 2021;**187**:976−87.
49. Fang CM, Ku MC, Chang CK, Liang HC, Wang TF, Wu CH, et al. Identification of endogenous site-specific covalent binding of catechol estrogens to serum proteins in human blood. *Toxicol Sci* 2015;**148**: 433−42.
50. McAulay K, Hoyt EA, Thomas M, Schimpl M, Bodnarchuk MS, Lewis HJ, et al. Alkynyl benzoxazines and dihydroquinazolines as cysteine targeting covalent warheads and their application in identification of selective irreversible kinase inhibitors. *J Am Chem Soc* 2020;**142**:10358−72.
51. Yang Y, Xiong Y, Zhu G, Sun M, Zou K, Zhao Y, et al. Discovery of seven-membered ring berberine analogues as highly potent and specific hCES2A inhibitors. *Chem Biol Interact* 2023;**378**:110501.
52. Wong DVT, Holanda RBF, Cajado AG, Bandeira AM, Pereira JFB, Amorim JO, et al. TLR4 deficiency upregulates TLR9 expression and enhances irinotecan-related intestinal mucositis and late-onset diarrhoea. *Br J Pharmacol* 2021;**178**:4193−209.
53. Wu Y, Cheng Y, Yang Y, Wang D, Yang X, Fu C, et al. Mechanisms of Gegen Qinlian pill to ameliorate irinotecan-induced diarrhea investigated by the combination of serum pharmacochemistry and network pharmacology. *J Ethnopharmacol* 2021;**276**:114200.